MICROROBOTS

A gyroscope-free visual-inertial flight control and wind sensing system for 10-mg robots

Sawyer Fuller^{1,2}*, Zhitao Yu¹, Yash P. Talwekar¹

Tiny "gnat robots," weighing just a few milligrams, were first conjectured in the 1980s. How to stabilize one if it were to hover like a small insect has not been answered. Challenges include the requirement that sensors be both low mass and high bandwidth and that silicon-micromachined rate gyroscopes are too heavy. The smallest robot to perform controlled hovering uses a sensor suite weighing hundreds of milligrams. Here, we demonstrate that an accelerometer represents perhaps the most direct way to stabilize flight while satisfying the extreme size, speed, weight, and power constraints of a flying robot even as it scales down to just a few milligrams. As aircraft scale reduces, scaling physics dictates that the ratio of aerodynamic drag to mass increases. This results in reduced noise in an accelerometer's airspeed measurement. We show through simulation and experiment on a 30-gram robot that a 2-milligram off-the-shelf accelerometer is able in principle to stabilize a 10-milligram robot despite high noise in the sensor itself. Inspired by wind-vision sensory fusion in the flight controller of the fruit fly *Drosophila melanogaster*, we then added a tiny camera and efficient, fly-inspired autocorrelation-based visual processing to allow the robot to estimate and reject wind as well as control its attitude and flight velocity using a Kalman filter. Our biology-inspired approach, validated on a small flying helicopter, has a wind gust response comparable to the fruit fly and is small and efficient enough for a 10-milligram flying vehicle (weighing less than a grain of rice).

Copyright © 2022 The Authors, some rights reserved; exclusive licensee American Association for the Advancement of Science. No claim to original U.S. Government Works

INTRODUCTION

The idea of extremely small autonomous robots, termed "gnat robots" (1, 2), first gained widespread attention in the 1980s. To provide a precise definition and terminology, we will define a Nature-inspired Aerial Ten-milligram robot, or "NAT robot," to refer to a robot that flies and weighs between 1 and 10 mg. A grain of rice weighs about 10 mg, making NAT robots smaller than the 100- to 600-mg flapping-wing flyers (weighing about the same as one to six toothpicks) that have been created to date, such as the Robofly (3-5), Robobee (6, 7), Bee+ (8), and Softfly (9) (Fig. 1). By virtue of their small size, NAT robots will have capabilities that distinguish them from larger robots. Operating in teams of thousands or millions, they could perform "fast, cheap, and out of control" space missions at markedly reduced launch cost, serve as autonomous mobile "smart dust" (10) to find hazardous fume sources or map air flow patterns, or collectively perform manipulation tasks on objects larger than themselves (11). Reduction in size to below 10 mg amplifies many of the scale-dependent benefits of small robots. These include greater deployment numbers at the same cost for improved coverage and the ability to harvest all needed energy from a greater array of ambient energy sources in the environment. The increasing surface area-to-volume ratio as scale diminishes favors solar power in small robots, for example (12). The ability to fly affords important benefits for small scale. These include easily surmounting obstacles (1) and the concomitant ability to come into closer proximity to sensing targets and power sources, lowering sensitivity and conversion efficiency requirements.

When sensing and control of such small flying vehicles is considered, the physics of small scale takes on a heightened importance

(13–16). For a robot of size scale ℓ (for example, its length from wing tip to wing tip), mass varies as ℓ^3 to first order. This implies that sensor mass must diminish as scale reduces, which rules out many sensor types for NAT robots and implies lower precision or update rates for others. It also places a severe limit on sensor and controller power, because battery mass also scales as ℓ^3 . As sensor quality degrades with scale, the speed of the dynamics they must control concomitantly increases. Angular acceleration and translational acceleration vary as ℓ^{-1} (if translational velocity is measured in units of body lengths per second or ℓ/s) (17). The attitude of small hovering vehicles, such as flapping-wing aircraft (18, 19), electrohydrodynamic (EHD) vehicles (20, 21), and flies (22), is unstable. This implies a size-dependent upper limit on sensor time delay or sampling rate (23). Together, these constitute extreme constraints on the speed, size, weight, and power (SSWaP) of a NAT robot's avionics system.

We addressed here the lowest level in the drone autonomy hierarchy introduced in (24), known as "sensor autonomy." Sensor autonomy entails the ability to hover in the air stably and is a requisite for higher-level tasks such as navigating through confined environments (25–31) and plume source seeking (32–34). Previous work in such avionics or "autopilot" systems geared toward small aerial vehicles has recognized the need for computation- and power-efficient onboard vision. A key constraint is power usage: We assumed that sensing and computation for a NAT robot must consume no more than 1 mW. This 10% of the power to fly, like previous visual flight demonstrations at 1.5 kg (31) and 30 g (35), assumes that a 10-mg NAT robot consumes a tenth of the 100 mW power needed for a 100-mg Robofly to fly (4). This rules out offboard sensor processing because wireless radio transmission consumes tens of milliwatts even for low-rate, low-resolution video (36). It also rules out emissive sensors such as laser rangefinders (1, 29) and sensors that require significant computation. The latter include signal processing for the Global Positioning System

¹Department of Mechanical Engineering, University of Washington, Seattle, WA, USA. ²Paul G. Allen School of Computer Science, Seattle, WA, USA. *Corresponding author. Email: minster@uw.edu

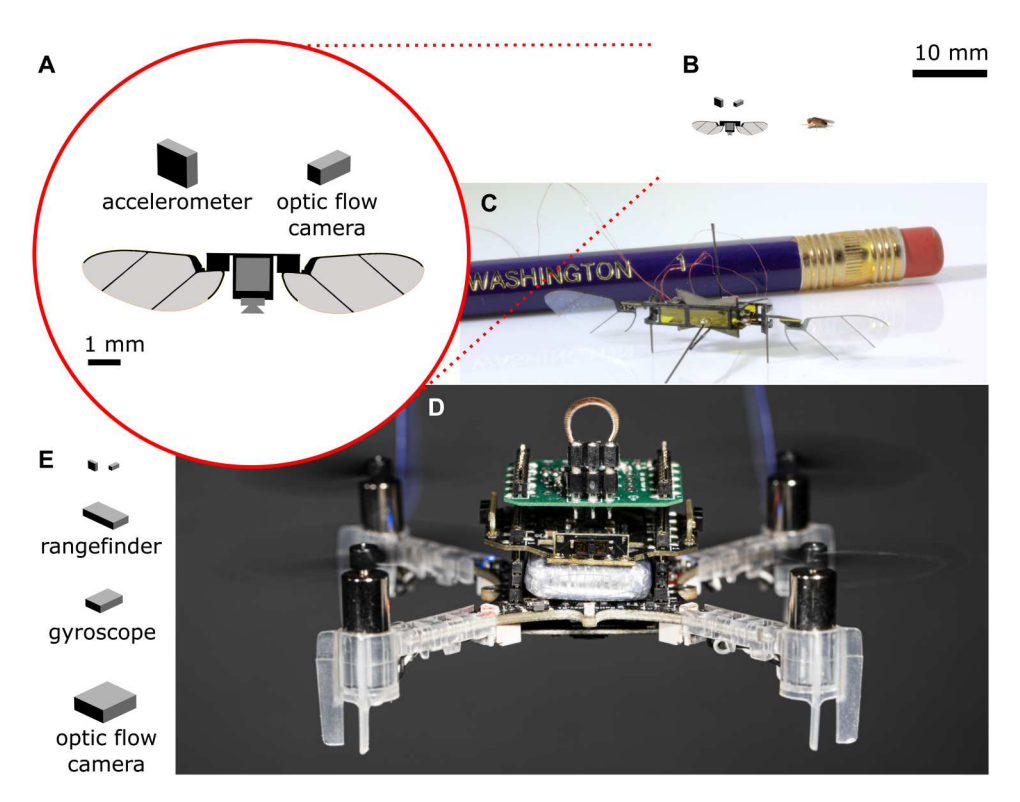


Fig. 1. The sensor suite and size of the conceptual nature-inspired aerial 10-mg "NAT" robot compared with other small aircraft. (A) Close-up view of the conceptual 10-mg robot and package sizes of its sensor suite made with off-the-shelf parts. Shown approximately to scale on the page are the (B) the NAT robot and its sensors along with the 1-mg fruit fly, (C) the 143-mg U. Washington Robofly (5, 104) with a pencil for scale, and (D) a palm-sized 30-g quad-rotor, the lightest vehicle yet to perform sensor-autonomous hover. Here, it is shown equipped with the moth-based odor sensor from (34) (copyright University of Washington). (E) Our proposed hovering sensors are much smaller and more power efficient than those used for autonomous hover in the palm drone (sensor package sizes also shown approximately to scale on the page).

and localizating relative to a stored map (e.g., simultaneous localization and mapping). Flight control using optic flow, a measure of the velocity of motion of visual scenery as the robot or animal moves through it, has been proposed as a low-power alternative (29, 31, 37–39).

The primary contribution here is an alternative avionics system with markedly reduced mass and power consumption that is nevertheless able to control such a vehicle. Our sensor suite is notable in that it eschews a heavy and power-hungry gyroscope, relying instead on a much lighter and more efficient accelerometer. The accelerometer is used to sense airspeed by sensing resultant drag-induced accelerations. Using this airspeed measurement and a model of the aircraft, it is possible to estimate attitude using a Kalman filter. We combined this with a power-efficient optic flow estimator, allowing the wind vector to be estimated as well. All elements of our system can be made using slightly modified versions of offthe-shelf components, implying that no untested technology is required. The sensors, computations, and controller together weigh about 6 mg in total and consume less than 200 µW on an off-theshelf microcontroller. This is achieved in part by computing exclusively using fast and power-efficient multiply and add operations. We show through analysis, simulation, and validation on a 30-g flying aircraft that the attitude estimate enables fast lateral maneuvers, and the wind estimate facilitates wind rejection. Our sensor suite also enables tasks, such as plume source finding, that rely on

knowledge of the wind vector, and it compensates for the attitude instability of small hovering aircraft.

RESULTS

The smallest drone yet to perform sensor-autonomous stable hover uses a sensor suite we will term gyroscope-rangefinder-optic flow (GRO). It combines a gyroscope (which measures angular velocity), a downward-facing rangefinder (which measures distance to the ground), and a downward-facing optic flow camera (which measures angular velocity of visual motion below the aircraft) (Fig. 1D) (40-42). Reference (41) describes the state estimator used on this palm-sized drone (Crazyflie, Bitcraze, Sweden) but with a different sensor suite that uses external position information. That system was subsequently updated to use GRO. The rangefinder in GRO can use sonar (40), RADAR, or LIDAR (distance-finding using the time to reflect for light) (41). It can be shown using the observability criterion (43) that GRO can observe a state given by q= $[\theta, \omega, v_x, z, v_z]^{\mathsf{T}}$ (see Fig. 2) (44). The key downsides of GRO are excessive weight and power consumption. The gyroscope must continually vibrate, making it weigh more and consume more power than an accelerometer, which uses a passive mechanical element. After decades of refinement, the lightest commercially available is the TDK Invensense ICM-20600, which weighs 15 mg and consumes at least 3 mW. Similarly, rangefinders consume energy because they must emit energy: The lightest (ST Microelectronics

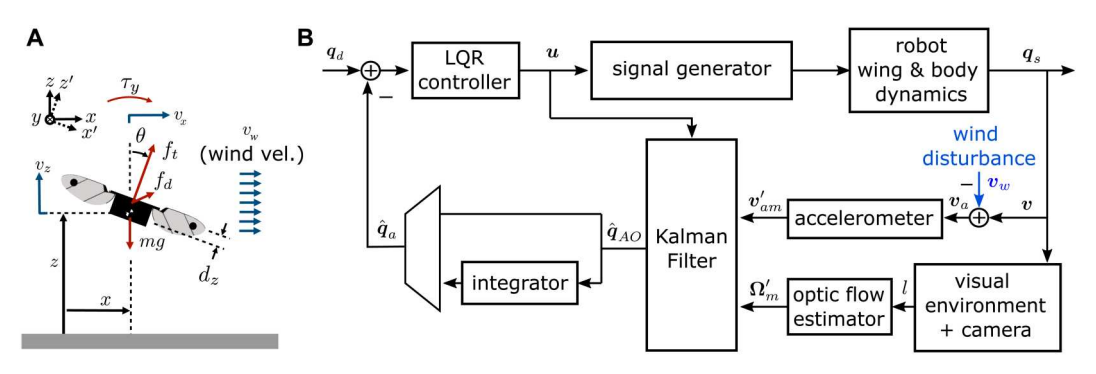


Fig. 2. Dynamics and flight control architecture overview. (**A**) Diagram of parameters that describe the dynamics of our model for a small hovering robot. (**B**) The proposed feedback control architecture is LQG (linear quadratic Gaussian), consisting of a linear quadratic regulator for a controller and a Kalman filter estimator. The sensor suite includes an accelerometer-based drag sensor that measures airspeed \mathbf{v}_{am} and a camera that provides a measurement Ω_m of the rate of optic flow. To estimate the states x, y, and z, the estimates of \mathbf{v}_{xv} \mathbf{v}_{vv} and \mathbf{v}_{zv} respectively, are numerically integrated.

VL53L0) weighs about 20 mg and consumes 6 mW (45). Together, the components of a GRO system, like the palm drone helicopter (Fig. 1D) (41), would weigh 134 mg and consume about 21 mW (Table 2). This far exceeds the capability of a NAT robot.

Sensor suite description

Here, we propose a markedly lighter and lower-power alternative to the GRO suite. Our system, which we call accelerometer-optic flow (AO), consists only of a three-axis accelerometer and an optic flow camera. These two devices are already available commercially in packages compatible with NAT scale (Fig. 1). The accelerometer, mCube MC3672 (mCube Inc., San Jose, CA, USA), measures about 1.1-mm square, weighs 2.0 mg, and consumes only about 20 μ W operating at 210 Hz. As for a camera, the commercially available OVM6948 (Omnivision Inc., Santa Clara, CA, USA) is light enough, measuring only 0.65 mm by 0.65 mm by 1.2 mm and weighing about 1 mg including its multielement lens. This camera consumes about 25 mW, exceeding the 1-mW NAT robot power budget. Imaging chips with suitable power usage and size

Table 1. Our conceptual AO sensor suite is markedly lighter and more efficient than the state-of-the-art small avionics system.

Component	Mass (mg)	Power (μW)
NAT	robot sensor suite (AO)	
Accelerometer	2.0	20
Optic flow camera	1.0	100 (47)
Microcontroller	3.2	48
Total	6.2	167
Palm o	drone sensor suite (GRO)	
Gyroscope	14	3000
Optic flow camera	97	12,000 (44)
Rangefinder	20	6000 (<i>105</i>)
Microcontroller	3.2	371 (44)
Total	134.2	21,371
Improvement factor	22 ×	128×

have been demonstrated in the laboratory, however. A 128 pixelby-128 pixel camera chip, operating at 10 frames/s, which consumes only 1 μW, has been created (46). Subsequent refinements made a more practical sensor with improved dynamic range and frame rate, at the expense of greater power usage, resulting in a 64 pixel-by-40 pixel sensor with an 80-dB dynamic range and 30-μW power consumption at 80 frames/s (47). These square sensors measure about 1 mm on a side and, through wafer thinning, can be made extremely lightweight. Commercial imagers now have the necessary efficiency: The Himax HM series (Tainan City, Taiwan) consumes 40 nW per pixel at 60 frames/s (fig. S1), suggesting a power usage of about 49 μW for a variant with a 35 pixel –by– 35 pixel imaging surface. A pinhole (48) or small spherical (36, 49) lens could also satisfy mass constraints. Compared with GRO, AO cannot observe altitude using a linear observer, but we discuss in the conclusion nonlinear methods that could be used to overcome this.

An airspeed sensor using an accelerometer

The fruit fly uses a sense of airspeed derived from the Johnson's Organs of its antennae, which detect deflections induced by wind (50). Wind sensors that are small enough or could conceptually be reduced in size to suit a NAT robot have been previously demonstrated but are not available off the shelf (51–55).

We build on previous work that used accelerometers to sense air drag to improve drone state estimation (56) and a later nonlinear observability analysis that showed that an accelerometer alone can estimate attitude and velocity (57). Here, we show that accelerometer performance for this task improves with diminishing scale, a promising route to attaining a state estimator compatible with the SSWaP constraints of a NAT robot.

Our approach uses an accelerometer to sense airspeed on a hovering robot. Note first that an accelerometer does not measure acceleration directly. Instead, it senses the "specific acceleration," which is the difference between its acceleration and acceleration due to gravity. Formally, the specific acceleration is $a_s = \frac{1}{m}(f - f_g)$, where m is the mass of the rigid body to which the accelerometer is attached, f is the sum of all forces acting on it, and f_g is the force of gravity. We assumed that the accelerometer is positioned near the aircraft's center of mass so that Coriolis accelerations are negligible. Now consider the accelerometer's reading in free fall. In the absence of air drag, it reads as zero because the only

force is gravitation, giving $a_s = \frac{1}{m}(f_g - f_g) = 0$, regardless of orientation (57). Now incorporate air drag while still in free fall. The accelerometer reads a nonzero value due to the aerodynamic drag force vector f_d , but gravitation cancels out as above, leaving $a_s = \frac{1}{m}f_d$. To model aerodynamic drag, define the airspeed as the difference between flight velocity v and wind velocity v_w (Fig. 2)

$$\mathbf{v}_a = \mathbf{v}_w - \mathbf{v} \tag{1}$$

We can use this information to estimate the airspeed if we have a model for how air drag maps to airspeed; that is, we know $f_d(v_a)$, for example, from wind tunnel tests (58). For a small flapping-wing robot, a number of lines of evidence point to a linear model

$$f_d(\mathbf{v}_a) = b\mathbf{v}_a \tag{2}$$

being a very good approximation for aerodynamic drag on flappingwing hovering aircraft and flies (59–64). The quantity b has been measured in a wind tunnel for both forward and lateral wind on the Robobee to be 2×10^{-4} Ns/m (59). It is 1.1×10^{-4} Ns/m for the 1-mg fruit fly in forward free flight, estimated by measuring flight velocity changes in response to wind gusts on flies whose wind-sensing apparatus was ablated (60).

Last, consider now that the aircraft to which the accelerometer is attached is subject to one additional force, a thrust force f_t caused by, for example, flapping wings. Then, total specific acceleration is given by $a_s = \frac{1}{m}(bv_a + f_t)$.

Now, rearrange this equation and express it body-attached coordinates, which are denoted by a () to distinguish from world coordinates. The airspeed is given by

$$\mathbf{v'}_{a} = \frac{m}{b}\mathbf{a'}_{s} - \frac{1}{b}\mathbf{f'}_{t} \tag{3}$$

This shows that the airspeed can be measured if the quantities m and b are known, the controller output f_i is known, and a_s is measured by the accelerometer. This formulation permits airspeed measurements even for aircraft that can actuate forward and lateral forces, which flapping wings are likely capable of (65), as well as advanced rotorcraft. This indicates that the accelerometer is nearly interchangeable with a flow-based sensor such as a whisker/antenna (52, 53) or Pitot tube, provided controller outputs are well known.

Here, without loss of generality, we assume that thrust only acts directly in line with the aircraft's z axis, that is, $f'_t = [0,0,f'_t]^T$, where f'_t is usually nearly equal to the gravitational force mg. In component form, the airspeed measurement is then

$$\mathbf{v'}_{a} = \left[\frac{m}{b} a'_{s_x}, \frac{m}{b} a'_{s_y}, \frac{m}{b} a'_{s_z} - \frac{1}{b} f'_{t} \right]^{\top} \tag{4}$$

Efficient optic flow estimation using autocorrelation

The other sensor modality we included is optic flow from an onboard camera, which measures the speed of visual motion. In the section on state estimation below, we show that a downward-facing optic flow camera can provide additional information about the rate of lateral motion that is necessary to estimate wind.

Here, we begin by considering the computations needed to estimate optic flow from pixel luminance readings taken by a camera attached to the robot. Suppose the camera collects luminance

readings $l(\gamma, t)$ (lux) at angles γ across a visual field. [This may be expanded to a two-dimensional (2D) surface by incorporating a second Euler angle β or by specifying a vector direction s on the unit sphere]. The simplest methods to estimate optic flow entail operations on the spatial luminance derivative $l_{\gamma}=\frac{dl}{d\gamma}$ (lux/rad, or the spatial gradient $\nabla_s l$ in 2D) and the temporal luminance derivative $l_t = \frac{dl}{dt}$ (lux/s) (66). In practice, the spatial derivative l_{γ} must be calculated by subtracting luminance readings at two nearby angles γ_1 and γ_2 separated by $\delta\gamma,$ such as at adjacent camera pixels, according to $l_{\gamma} = \frac{1}{\delta \gamma} (l(\gamma_2) - l(\gamma_1))$. The time derivative is calculated by subtracting successive luminance readings (camera frames) at times tand $t - \delta t$, according to $l_t = \frac{1}{\delta t}(l(t) - l(t - \delta t))$, where δt is the time interval between frames. Assuming that the shape of the luminance image remains fixed between frames but moves by a small amount, the measured optic flow along one dimension for a single pixel pair can be computed according to $\Omega_m = -l_t/l_v$. This is a special case of the Lucas-Kanade method (67), which is a simple and accurate method to estimate the average 2D optic flow in an array of pixel readings (66).

In the 2D case, arrays of derivatives are constructed in which each entry corresponds to a pixel in the camera: l_s consists of pairs of spatial derivatives along two linearly independent directions (e.g. $[l_{\gamma}, l_{\beta}]$), and l_t consists of temporal derivatives for each pixel. The Lucas-Kanade method for both 1D and 2D estimates optic flow in a least-squares sense according to

$$\Omega_m = -(\boldsymbol{l}_s^{\top} \boldsymbol{l}_s)^{-1} \boldsymbol{l}_s^{\top} \boldsymbol{l}_t \tag{5}$$

In pursuit of minimizing the computation required to estimate optic flow, we consider a simplification inspired by biology, which has been previously proposed (68), that requires fewer operations. It is given by

$$\Omega_m = c \mathbf{l}_s^{\mathsf{T}} \mathbf{l}_t \tag{6}$$

where c is a scalar constant. Because it entails only multiplication, it is often called "autocorrelation," or "a correlator" for short. In Lucas-Kanade, c is computed each frame according to $c = -(\boldsymbol{I}_s^{\top} \boldsymbol{I}_s)^{-1}$. This more than doubles the multiply-add operations and requires a division operation to invert the 2×2 matrix. Equation 6 is a slight variation on the Hassenstein-Reichardt model for insect optic flow processing (69) (see the Supplementary Materials).

Observing attitude, velocity, and wind speed

We show that the accelerometer-only sensor suite is able to estimate the aircraft attitude and velocities. Then, we incorporate the optic flow sensor, creating the AO sensor suite that can additionally estimate wind speed ν_w .

Dynamic model

We describe a dynamic model for the aircraft that is an integral part of our Kalman-based state estimator and closed-loop simulation. Figure 2 depicts forces acting on a flapping-wing robot such as a NAT robot or the Robofly, but the proposed model can apply to almost any small hovering aircraft, including multirotor drones and EHD-based thrusters (21). For a flapping-wing or rotor-

actuated aircraft, air drag is about linear with airspeed (Eq. 2) (59, 60, 70). For non–flapping-wing devices near hover conditions such as EHD-actuated aircraft (20, 21), drag is dominated by inertial flow, which varies as the square of airspeed instead of linearly with it. For these, a reasonable linear model has b=0.

For control and estimation, linearity of airspeed drag results in a good linear approximation of the vehicle's dynamics (59, 61, 62). For a state given by

$$\boldsymbol{q}_{s} = [\theta, \omega, x, \nu_{x}, z, \nu_{z}, \nu_{w}]^{\top}$$
(7)

and inputs being the body–z-axis translational acceleration and body–y-axis angular acceleration (Eq. 20), the linearization of the dynamics in (17) has the form $\dot{q}_s = Aq_s + Bu$; $y = Cq_s$, where the Jacobian linearization is taken at $\theta = \omega = v_x = v_z = 0$, $f_t = mg$. The position $p = [x, z]^{\mathsf{T}}$ has no effect on the Jacobian. The resulting matrices are given by

$$A = \begin{bmatrix} 0 & 1 & 0 & 0 & 0 & 0 & 0 \\ 0 & -\frac{c}{J} & 0 & -\frac{b}{J}d_z & 0 & 0 & \frac{b}{J}d_z \\ 0 & 0 & 0 & 1 & 0 & 0 & 0 \\ g & -\frac{b}{m}d_z & 0 & -\frac{b}{m} & 0 & 0 & \frac{b}{m} \\ 0 & 0 & 0 & 0 & 0 & 1 & 0 \\ 0 & 0 & 0 & 0 & 0 & -\frac{b}{m} & 0 \\ 0 & 0 & 0 & 0 & 0 & 0 & 0 \end{bmatrix};$$

$$(8)$$

$$B = \begin{bmatrix} 0 & 0 \\ 1 & 0 \\ 0 & 0 \\ 0 & 0 \\ 0 & 0 \\ 0 & 1 \\ 0 & 0 \end{bmatrix}$$

where J is the moment of inertia of the vehicle and c is its damping due to angular velocity (see Materials and Methods). This linear dynamical system exhibits the growing oscillatory instability that is characteristic of small flapping-wing vehicles (18, 61).

Accelerometer-only observability

As above, for simplicity of exposition, we consider a simplified system consisting only of planar, 2D motion as depicted in Fig. 2. The accelerometer system output is defined as the body x and z axis components of the accelerometer's airspeed measurement (Eq. 4), given by

$$\mathbf{y}_{A} = \begin{bmatrix} \mathbf{v'}_{a_{x}} + n_{a} \\ \mathbf{v'}_{a_{z}} + n_{a} \end{bmatrix} \tag{9}$$

where each n is sensor noise added to the reading, which we assume is zero-mean Gaussian white noise. The state vector to be estimated is given by

$$\boldsymbol{q}_{A} = \left[\theta, \omega, \nu_{x}, \nu_{z}\right]^{\top} \tag{10}$$

The accelerometer-only sensor suite is not able to estimate with wind speed v_w , so we assume that it is zero and leave it out of the state. The Jacobian linearization of the measurement model (Eq. 9),

taken at hover, is given by

$$C_A = \begin{bmatrix} 0 & 0 & -1 & 0 \\ 0 & 0 & 0 & -1 \end{bmatrix} \tag{11}$$

The dynamics matrix associated with this estimator, A_A , is the A matrix in Eq. 8 with rows and columns associated with x, z, and v_w removed. The observation matrix (43) obsv(A_A , C_A) is full rank, indicating that the entirety of the state vector \mathbf{q}_A can be observed in a neighborhood of upright hover. Given that the system can be observed, a Kalman filter–based linear estimator with dynamics of the form

$$\dot{\hat{\mathbf{q}}} = A\hat{\mathbf{q}} + B\mathbf{u} + L(\mathbf{y} - C\hat{\mathbf{q}}) \tag{12}$$

can be constructed to estimate the state of the system. In the accelerometer-only sensor suite, the state to be estimated is q_A (Eq. 10).

Using optic flow to additionally observe wind velocity

We added a downward-facing camera (pointed in the negative of the body z direction, that is, along -z') to provide a second measure of lateral velocity that is not affected by wind, unlike the accelerometer. The optic flow camera uses either autocorrelation or Lucas-Kanade to provide a measurement Ω_m of the true optic flow Ω . Formally, optic flow is the time rate of change of a unit vector s pointed in the direction of a given visual feature as it moves across the visual field (37).

It can be shown that the x' component (defined in the body frame) of the optic flow sensed by a downward-facing camera is given in (37)

$$\Omega = \omega - \frac{\cos\theta}{2} \nu'_{x} \tag{13}$$

This shows that the sensor provides information about the body frame lateral velocity v'_{xy} but its output is also affected by other state variables ω , θ , and z. Under conditions when $\omega = \theta = 0$ (as would occur during stable, level flight), the optic flow is simply $\Omega = v_x/z$, which can be used to estimate velocity if the altitude z is known (29). However, this is a restrictive assumption, and current barometric altimeters are too heavy and consume too much power for a NAT robot (ST, Bosch, Omron, Murata, and TDK only market $>2 \times 2$ mm packages, e.g., the 2×2 Bosch BMP390 weighs 6.3 mg and consumes 1.1 mW at 50 Hz). The observability criterion given below shows that even under more general conditions, when combined with the accelerometer, the additional information provided by optic flow can be used to estimate and reject the effect of a wind disturbance.

The output "measurement model" for the combined AO sensor suite is given by

$$\mathbf{y}_{\mathrm{AO}} = \begin{bmatrix} v'_{a_x} + n_a \\ v'_{a_z} + n_a \\ \Omega + n_s \end{bmatrix} \tag{14}$$

where each n is zero-mean Gaussian white sensor noise.

We assume that the wind velocity v_w only acts in the world x direction, which is why it is only a single state. To estimate this quantity, we introduce an augmented state that includes the wind velocity

$$\boldsymbol{q}_{\mathrm{AO}} = \left[\theta, \omega, \nu_x, \nu_z, \nu_w\right]^{\top} \tag{15}$$

The optic flow measurement depends on altitude, so we take the Jacobian linearization at a specific desired altitude z_d , giving

$$C_{\text{AO}} = \begin{bmatrix} 0 & 0 & -1 & 0 & 1\\ 0 & 0 & 0 & -1 & 0\\ 0 & 1 & -\frac{1}{z_d} & 0 & 0 \end{bmatrix}$$
 (16)

The observability criterion indicates that q_{AO} is observable, including the wind velocity. As above, we use the Kalman filter (12) to provide the estimate \hat{q}_{AO} .

For some tasks, it is desirable to stabilize to a desired position. To provide a coarse position estimate for use in control, we numerically integrated the estimates \hat{v}_x and \hat{v}_z according to the last line in Eq. 21 (Supplementary Materials) to obtain an augmented state \hat{q}_a that includes \hat{x} and \hat{z} estimates. These two states are not technically "observable," meaning that their estimates will slowly drift over time as sensor noise numerically accumulates. However, their presence allows, for example, performing lateral maneuvers of a desired distance.

State estimator and flight controller

Anticipated sensor noise plays an important role, so we formulate the feedback system as an LQG (linear quadratic Gaussian) control problem. The system is underactuated, but the controllability matrix ctrb(A, B) (43) is full rank, showing that the system is controllable. We constructed a trajectory-following LQR controller to follow a (slowly varying) desired reference trajectory $\boldsymbol{p}_d(t) = [x_d(t), z_d(t)]$ using the controller

$$\mathbf{u} = K(\mathbf{q}_d - \hat{\mathbf{q}}) \tag{17}$$

The combination Kalman filter and LQR controller is known as an LQG regulator and is diagrammed in Fig. 2.

The LQR controller includes an additional component to compensate for wind. To move laterally, the LQR controller effectively makes the robot perform "helicopter-like" control, tilting so that the thrust from the wings f_t takes on a lateral component (Fig. 2). Assuming lift balances gravity, the lateral thrust is $mg\sin\theta \approx mg\theta$, which can be produced through suitable choice of set point θ . In the presence of a nonzero wind estimate \hat{v}_w (only possible with

the AO sensor suite), the torque and attitude commands are altered to compensate for the added translational drag force accord-

ing to
$$\theta_d = \theta_d - \frac{b\hat{v}_w}{mg}$$
 and added torque according to $\tilde{\tau}_y = \tilde{\tau}_y - \frac{d_z b\hat{v}_w}{I}$.

Noise scaling in accelerometer-based wind sensing

A key concern in the design of the NAT robot's sensor suite is that high sensor noise magnitude could result in sluggish performance in the estimator, or worse, instability if the control loop is operated at a low rate. Typically, smaller and lower-power sensors have lower performance. For example, the 2-mg mCube MC3672 accelerometer on the NAT robot has a 2.5× higher root mean square (RMS) noise than the 30-mg Bosch BMI088 in the drone (Table 1). Our results show that despite this, our conceptual NAT robot senses airspeed with a much lower noise magnitude than larger aircraft because of favorable scaling physics. As scale reduces, the acceleration per unit airspeed, which is parameterized by the ratio b:m, increases as a result of decreasing wing loading with scale (71). It follows a roughly inverse quadratic trend $\frac{b}{m} = 0.15 m^{-1.9}$ over nearly five orders of magnitude (Fig. 3A). When used as an airspeed sensor, the accelerometer's sensor noise SD is given by $\sigma_a = \frac{m}{h} \sigma$, where σ is the SD of the acceleration measurement. The noise magnitude diminishes as scale reduces (Fig. 3B). Table 1 shows that despite its noisier accelerometer, a NAT robot with a scale-appropriate b:m ratio using the fit exponential given above has nearly $5\times$ lower airspeed sensing noise. Details are provided in the Supplementary Materials.

Closed-loop visual flight control in simulation

Figure 4A shows a trajectory of the system in closed loop using only accelerometer feedback (no vision), indicating the feasibility of trajectory control. The figure shows the effect of realistic conditions in which the initial condition of the estimator does not match the true state.

Figure 4C shows that the proposed autocorrelation method has similar performance as Lucas-Kanade. Figure 4D and fig. S2 show

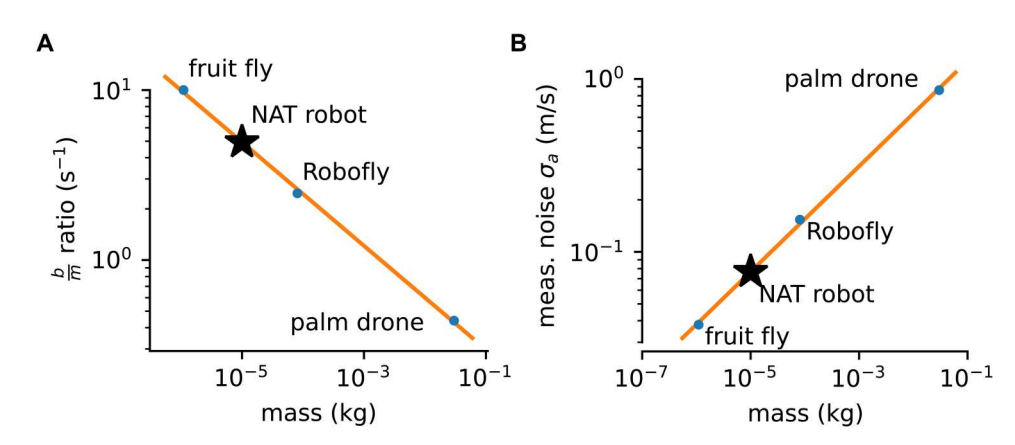


Fig. 3. Scaling laws in accelerometer-mediated wind sensing reduce the airspeed measurement noise as size reduces. (A) The ratio of damping to mass varies approximately with the inverse square of mass, with a least log-error exponential fit giving $\frac{b}{m} = 0.15m^{-1.9}$. (B) This results in reduced airspeed measurement noise σ_a as size diminishes.

Table 2. Small scale allows the NAT robot to sense airspeed with lower noise than a palm drone despite more noise in the sensor itself.

	NAT robot	Palm drone	Units
Mass (m)	10	30,000	mg
Air drag coefficient (<i>b</i>)	49.4×10 ⁻⁶	13.2×10 ⁻³ (<i>103</i>)	Ns/m
Acceleration per unit airspeed (b : m)	4.9	0.44	s ⁻¹
Noise (amplitude spectral density)	Not provided	175	μgee Hz ^{-½}
RMS accel. noise, 100 Hz (σ)	4.4	1.75	milli-gee
RMS accel. noise, 200 Hz, in flight	0.38	0.15	m/s ²
RMS airspeed noise (σ_a)	0.077	0.34	m/s

that our proposed system under closed-loop LQG control using autocorrelator-based optic flow estimation is able to reject a simulated step change in wind speed in slightly more than a second.

Power and mass

Tables S1, S2, and S3 tally the necessary operations per second and power required to perform flight control using the two optic flow methods. Lucas-Kanade and autocorrelation perform comparably (Fig. 4) and operate within the required 1-mW power budget when executed on an off-the-shelf microcontroller, but the autocorrelation method uses about a third as much power. Table 2 provides the estimated mass and power consumption of the complete AO sensor and control system. Masses of each component were taken using a precision scale with a 0.1-mg resolution. We searched for the lightest gyroscope (TDK Invense ICM20600) and accelerometer (Mcube MC3672) commercially available and took estimated power numbers from the corresponding datasheets. Power usage of the AO camera, the optic flow camera, and rangefinder was measured in the citations provided. We have neglected the mass of a flex circuit and additional required discrete components, which tends to add an additional 25% (44). Even when compared with a version of the drone's GRO suite with the most recent (lighter) version of each sensor, AO is substantially lighter and more power efficient. More details are provided in the Supplementary Materials.

Physical robot validation

To demonstrate that the accelerometer itself can directly measure lateral velocity, we collected data from a 30-g palm-sized four-rotor helicopter (Crazyflie 2.1, Bitcraze, Sweden) (see Materials and Methods). No Kalman filter was used in this test. Figure 5A shows that our accelerometer-based lateral velocity estimate corresponds well to the true lateral velocity provided by the palm drone's full, GRO-based state estimator when undergoing lateral motions along both the *x* and *y* directions. The inclination of the helicopter is small, just a few degrees, so we are able to compare the body frame accelerometer–based velocity estimate with the world-frame state estimator's lateral velocity, although they are in different frames. The accelerometer-based wind estimate does not appear to be distorted by flight-induced vibrations.

We then constructed a Kalman filter–based estimator to validate the ability of our AO-based avionics suite to estimate both wind and aircraft attitude. Figure 5B shows a comparison of the measured wind speed from a hot-bulb anemometer (Testo 405, West Chester, PA USA) with our system's estimate. Important features of the wind speed measurement from the anemometer can be observed in our estimate, including onset time, peaks, and the slow decay of the wind after the fan was powered down. Our system's attitude estimate also follows the prediction by a lateral force $(-bv_w)$

balance
$$\theta = \arcsin\left(\frac{-bv_w}{mg}\right)$$
.

Comparison with the fruit fly's wind gust response

Last, we compared the performance of our system with behavioral data collected from the fruit fly Drosophila melanogaster subjected to rapid, impulsive gusts of wind provided by an air piston while they flew along a wind tunnel with a 30-cm-square cross section (60). A purely passive simulated mass with the same b:m ratio as the fly and our conceptual NAT robot (10.0 s⁻¹) initially moves with the gust before returning to zero velocity. By contrast, both the fly's mean velocity response (n = 92) and our AO flight controller responded initially by moving more vigorously in the direction of wind than the passive particle (Fig. 6 and fig. S3). This indicates that both use a feedback regulator that senses wind and attempts to regulate flight speed by minimizing airspeed error. Both also exhibit a delayed compensatory response that overshoots, leading to a positive value of v_x for a short period of time after t > 0.3 s. This is the result of a compensatory visual feedback response that is slower because visual feedback is noisier than wind feedback for our system and likely the fly as well (72). The dynamics are also affected by coupling between forward thrust and the rotational pitch dynamics.

DISCUSSION

The avionics for a 10-mg flying robot is subject to extreme SSWaP constraints. Here, we introduce three innovations that drastically lower the mass and power of sensors required to hover while retaining sufficient bandwidth to stabilize. The first is to show that, because acceleration due to air drag on small aircraft is high, an accelerometer constitutes a light, precise, and power-efficient means to sense airspeed on smaller aircraft. This was inspired by previous work showing that an accelerometer can sense airspeed on drones (41, 56, 57). The second is the use of a fly-inspired autocorrelation algorithm to reduce the computation needed for optic flow processing. Because our Kalman filter observer also estimates angular velocity, it effectively derotates the optic flow measurement. Our entire flight controller operates exclusively using power-efficient multiply and add operations. The third is to combine these elements to solve the key problems of attitude and wind estimation. By estimating these quantities, the robot is able to make rapid maneuvers and reject the effect of wind. Knowledge of the wind vector also facilitates higher-level capabilities such as plume source finding (34). The stable hovering platform and autocorrelator-based optic flow system described here serve as a foundation upon which higherlevel "reactive autonomy" tasks can be performed.

Our results show that by using only an accelerometer and camera, the avionics system mass is reduced by more than 20-fold and power usage reduces by more than 100-fold compared with previous demonstrated hovering controllers. This work represents an

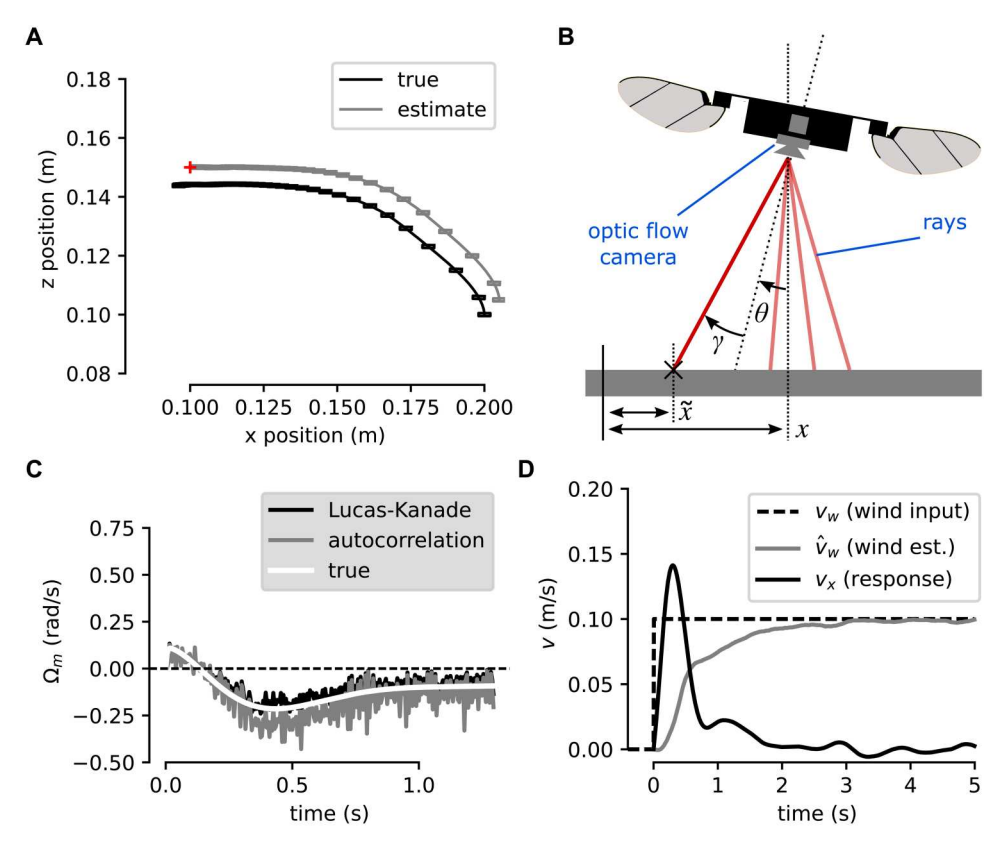


Fig. 4. Simulation results. (**A**) Flight path of the accelerometer-only sensor suite along the *x* and *z* dimensions. The aircraft performs a lateral maneuver starting at the lower right to a set point location (red cross mark) on the top left. The true trajectory is shown in black; the state estimate (gray) is subject to an error in the initial estimated position but is able to nonetheless maintain attitude stability. Lines show the path of the center of mass, and boxes depict the vehicle's approximate size and attitude at 200-ms intervals. (**B**) Diagram of the camera model in the accelerometer-optic flow (AO) sensor suite: Luminance readings $I(\gamma)$ are collected at uniformly spaced angles γ (red lines), which intersect a texture projected on the ground below at a position $\tilde{x} = x - z \tan(\gamma + \theta)$. (**C**) The correlator method produces similar output to Lucas-Kanade-based optic flow estimation when following the same (arbitrary) trajectory. (**D**) The simulated AO system, when using autocorrelation-based optic flow estimation, is able to sense and react to a wind disturbance. A step change in wind speed causes the aircraft to initially move in the direction of the wind. After about a second, the wind estimate has converged on its true value; the controller responds by commanding the robot to incline itself, resulting in a nearly perfect rejection of the disturbance.

important step toward realizing 10-mg aerial robots first conjectured in (1), as well as significantly reducing sensor mass and power for 100-mg robots like the Robofly (3, 4). We validated our results on a 30-g palm-sized hovering rotorcraft. Our system was inspired by how the 1-mg fruit fly *D. melanogaster* combines airspeed and visual feedback to navigate wind and exhibits an impulsive wind gust response that closely resembles it.

Compared with (29) and (73), our wind-vision sensor fusion does not require a power-hungry gyroscope to derotate the optic flow and can operate at hover rather than stable forward flight. This makes it far more suitable for very small aircraft, which, like small insects and hummingbirds, must hover because of a low-glide ratio (74, 75). Both the present work and (39) propose lightweight sensor systems based on optic flow to estimate attitude and velocity. Ours uses an accelerometer to additionally estimate wind speed, whereas (39) shows that nonlinear estimation can in principle eliminate inertial sensors entirely though flight demonstrations required a gyroscope.

The present work is motivated by a larger narrative of advancements in ultratiny flying robots. Flapping systems of 1 to 5 mg have been demonstrated (76–78). Actuators for small robots are largely electrostatic, requiring high voltages. A controllable coil-based

voltage boost converter has been realized (79); a long series of photovoltaic cells is another option (80). Milligram batteries have been fabricated by 3D printing (81), photolithography (82), and laser microfabrication (83). Recent results indicate that it may be possible to dispense with the battery together using solar cells, which can be extremely thin and have a favorable surface area—to—volume ratio as scale reduces (12).

The physical sensor suite proposed here satisfies proposed SSWaP constraints (\approx 6 mg, <1 mW, >200 Hz) using an off-the-shelf accelerometer combined with efficient imaging sensor technology that has been demonstrated in the literature, such as sub–100- μ W sensors (46, 47) and commercially in the Himax HM series. Such imagers could be combined with small optics such as the multielement lens in the \approx 1-mg Omnivision OVM6948 camera. Cameras with integrated optic flow estimation hardware (84, 85) and event cameras (86) have the potential to reduce both power and latency even further below what is possible with the camera-and-computer architecture considered here.

A linear observer is unable to estimate both the altitude and wind velocity using the AO sensor suite introduced here. This is in contrast to GRO, which is able to by virtue of its emissive (powerhungry) rangefinder (40). A number of methods have been

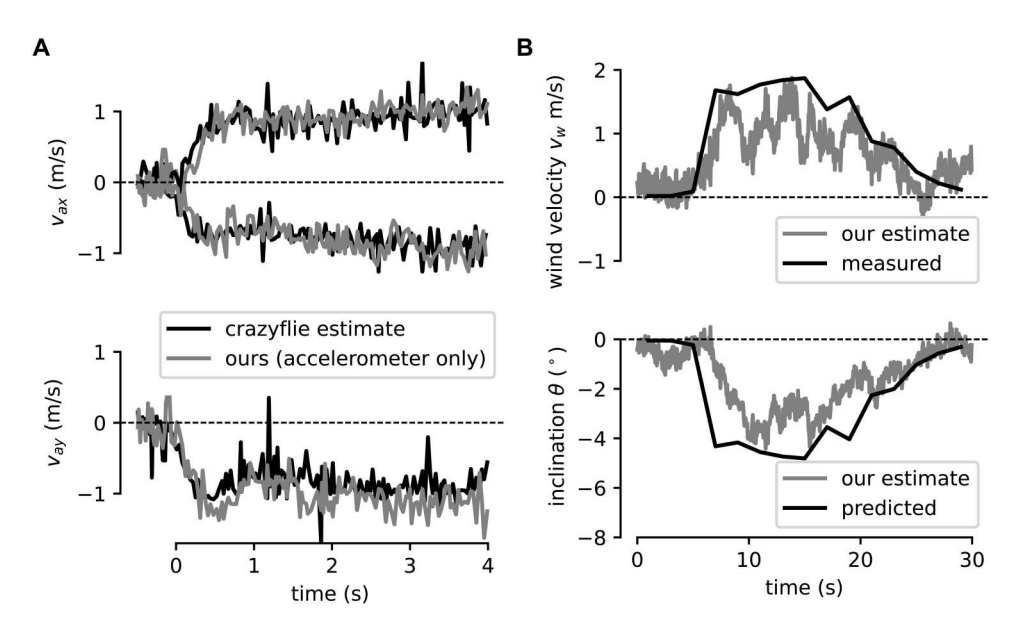


Fig. 5. Flight tests on a 30-g palm drone show that our accelerometer-vision system can estimate vehicle state and wind speed. (A) We used the accelerometer alone (no Kalman filter) to measure airspeed v_a in still air (v_w = 0), providing an estimate of lateral velocity $v = -v_a$ in both the x and y directions during a rapid lateral maneuver. Estimates are very close to the helicopter's full GRO-based state estimate. (B) The full AO sensor suite and Kalman filter estimator are able to estimate the wind velocity induced by a fan with reasonable performance, as well as the aircraft's attitude.

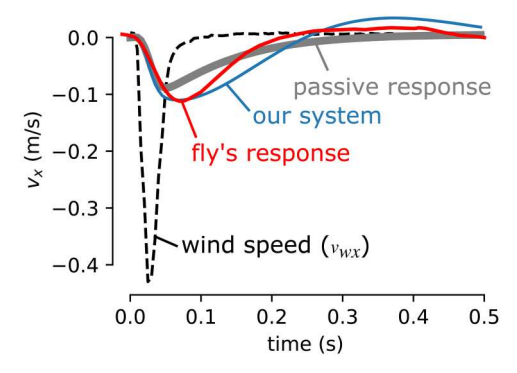


Fig. 6. Our simulated AO 10-mg aircraft when operated in closed loop (blue), has a velocity response to an impulsive wind gust that closely resembles that

of fruit flies. For this simulation, we set $\frac{b}{m}$ to equal the 10.0 s⁻¹ measured in 1-mg fruit flies. Compared with a passive response of a particle suspended in air (gray), both our system (blue) and the fly (red) have similar dynamics, exhibiting a larger impulse response followed by a delayed compensatory overshoot beginning after about 0.2 s. The red line is the mean velocity response of fruit flies flying along the length of a wind tunnel [n = 92, from (60)].

proposed in the literature that would not require additional hardware to control altitude (87). The first is to take advantage of the ground effect, which is an increase in lift that occurs near the ground, to obtain an altitude equilibrium (28). Another is to include a feedback law that varies thrust f'_t rather than inclination angle θ in response to optic flow. This can regulate altitude through a suitable optic flow set point (30, 88). A third is to detect delay-induced feedback instability in an optic flow–mediated altitude controller (89). A widely varying altitude requires modification of our linear estimator to accommodate the associated optic flow nonlinearity in z in Eq. 13. Two alternatives are an extended Kalman filter

at the cost of an additional $\approx 200 \,\mu\text{W}$ (44) or to use a "gain-scheduled" Kalman filter at negligible additional power.

We have neglected some nonidealities in physical accelerometers, such as bias drift (90), which will manifest in a larger magnitude of lateral drift velocity. We anticipate that the reactive-autonomy layer or nonlinear methods can be used to compensate (91). For example, an omnidirectional camera could be used to stabilize a single position using visual servoing (92), avoid walls (29, 30, 93), or navigate confined spaces (28, 30, 35, 94, 95). Chemical sensors can be added to seek chemical plume sources (34) or map them (33).

Our system responds similarly to the fruit fly to gusts of wind in flight. This indicates desirable real-world performance. Our results also provide insight into the mechanisms used by insects for their superlative flight abilities (96, 97). An open question is how animals like bees and moths stabilize their flight without the gyroscopic halteres carried by dipteran flies (98). One possibility is sensing twisting motions in the hind wings (99). Our results suggest that what we believe represents an alternative testable hypothesis. We suggest that it is possible that these animals could estimate and therefore stabilize their attitude by sensing airspeed using their wind-sensitive antennae (50, 60). An airspeed sense mediated by these organs could in principle provide the exact same feedback as the accelerometer-mediated airspeed sensing described here.

MATERIALS AND METHODS

Dynamic model

We created a nonlinear flight dynamic model to simulate NAT robot flight motion and to construct the linearized dynamic model used in its state estimator. For many hovering aircraft, the center of aerodynamic drag force is displaced by a vector d_z relative to the center of mass (Fig. 2), which results in a torque-force coupling. If this is the case, a slight modification of our air drag model

in Eq. 2 is needed, which is given by

$$\boldsymbol{f}_d = b(\boldsymbol{v}_w - \boldsymbol{v} - \boldsymbol{\omega} \times \boldsymbol{d}_z) \tag{18}$$

where ω is the angular velocity vector of the vehicle. The resulting drag torque is given by $\tau_d = d_z \times f_d$. Whether d_z is zero length does not affect either the observability or controllability of our system discussed below, but its effect was included to provide a more faithful model of many real-world aircraft. An aerodynamic rotational damping coefficient c adds rotational drag according to $\tau_{dy} = -c\omega_y$. It can be shown that $c = bd_z^2 + bd^2$ for the roll axis and $c = bd_z^2$ for the pitch axis (62), where d is the lateral distance from the center of mass to the center of aerodynamic pressure of the wing (denoted by a dot in Fig. 2).

To simplify exposition and analysis, we assume that yaw angle is controlled to have a near-zero yaw rate, which has previously been demonstrated on an insect-sized flapping-wing robot (5). With this assumption and an assumption that the moment of inertia matrix **J** is diagonal, cross product terms in the Euler-Lagrange equations (see the Supplementary Materials) can be neglected. If the attitude remains near upright ($\theta = 0$), then the dynamics reduce to two nearly independent planar systems with three degrees of freedom, that is, motion and rotation in the *x-z* and *y-z* planes, each of which can be controlled independently (61, 100). Hence, our nonlinear 2D-simulated dynamical system is a simplified version of Eq. 2 given by

$$\dot{\theta} = \omega$$

$$\dot{\omega} = \frac{1}{J} (b d_z \times f_d - c \omega + \tau_y)$$

$$\dot{\mathbf{v}} = \begin{bmatrix} 0 \\ -g \end{bmatrix} + \frac{1}{m} f_d + \frac{1}{m} \mathbf{R} \begin{bmatrix} 0 \\ f'_t \end{bmatrix}$$

$$\dot{\mathbf{p}} = \mathbf{v}$$

$$\dot{\mathbf{v}}_w = 0$$
(19)

where f_d is given in Eq. 18, $p = [x, y, z]^{\top}$ is the position of the center of mass of the robot in world coordinates, and \mathbf{R} is the rotation matrix that relates vectors given in body-attached coordinates to world coordinates. For any vector \mathbf{v} expressed in world coordinates, \mathbf{v} is the same vector expressed in body-attached coordinates. They are related by $\mathbf{v} = \mathbf{R}\mathbf{v}$. The wind velocity state v_w (Fig. 2) is included because the Kalman filter estimates it. For the 2D case, we use that $\mathbf{R} = [\cos\theta, \sin\theta; -\sin\theta, \cos\theta]$. The gravitational force is given by $f_g = [0,0, mg]^{\top}$.

If thrust is generated by a pair of thrusters, such as two wings or a pair of EHD thrusters, thrust force f_t and control torque τ_y are actuated independently by inverting the relations $f_t = f_1 + f_2$ and $\tau_y = d(f_1 - f_2)$, where f_1 and f_2 are thrust forces applied by the left and right thruster, respectively. We define the inputs to be

$$\boldsymbol{u} = \left[\tilde{\tau}_{y}, \tilde{f}_{t}\right]^{T} \tag{20}$$

where \tilde{f}_t is any change in thrust relative to the baseline needed to compensate exactly for gravity, scaled to have units of acceleration (ms⁻²), that is, $\tilde{f}_t = f_t/m - g$. Similarly, $\tilde{\tau}_y = \tau_y/J$ is the normalized input torque that has units of angular acceleration (rad s⁻²).

Python-based simulation environment

Many elements of our analysis were facilitated by simulation. We created a simulated NAT robot using Python and the Python Control Systems Library (101) using a fixed-step Euler integrator at 200 Hz to solve the 2D version of the Euler-Lagrange dynamics equations in Eq. 19, the linear feedback controller in Eq. 17, and the Kalman filter dynamics in Eq. 12 in the *x-z* plane. All software used to create the figures is released as open source on Github using a persistent Digital Object Identifier at https://doi.org/10.5281/zenodo.7324484.

For the AO sensor suite, which includes a camera, we additionally constructed a simple visual environment, camera model, and added wind input. We used a ray casing algorithm to read pixel luminance values from a 1D visual image textured on the ground, as depicted in Fig. 4. The texture is a single line of pixels extracted from a photograph of an outdoor scene. The optic flow measurement Ω_m of our camera was calculated using Eq. 6 over an array of 35 luminance readings arrayed evenly over a region $\gamma = (-15^\circ,15^\circ)$ directly below the robot, captured at the update rate of 200 Hz. At the start of the simulation, we computed the value of c in Eq. 6, which is a measure of the average gradients in the projected image, using $c = -(l_c^{\top} l_s)^{-1}$.

The weighting matrices for the Kalman filter were derived as follows. The variance of noise n_a in the airspeed estimate is the square of the RMS noise derived in Fig. 3. We manually tuned the optic flow noise to be much higher than was observed in simulation to provide for conservative performance. Disturbance magnitudes were hand-tuned. For the LQR controller, thrust and torque effort were balanced approximately by power used; state cost was manually tuned. We computed the gains K and L using the Python Control System Library (101). Values for these matrices were the same for all simulations. In practice, it may be desirable to incorporate an integral action term on θ to reject disturbances from a wire tether or manufacturing irregularity (7, 102).

Robot platform

We performed tests on a small (palm-sized) quad-rotor helicopter (Crazyflie 2.1, Bitcraze, Sweden) in an indoor environment, both in wind-free conditions and in the presence of a fan. We collected sensor information over Bluetooth from the helicopter as it flew. The helicopter was equipped with a downward-facing rangefinder, gyroscope, and optic flow camera (the GRO sensor suite) that it used to estimate its velocity and position using an extended Kalman filter (41). A careful analysis of its open-source software, confirmed by its author, shows that it does not use the x and y axis measurements of its accelerometer for state estimation in free flight. Our airspeed measurement assumes that $b = 13.2 \times 10^{-3}$ Nm/s, which was empirically tuned and is in a similar range to the 6.6×10^{-3} Nm/s estimated in a system identification effort (103). We used m = 30 g from the datasheet of the device.

For the direct airspeed measurements, no Kalman filter was used, and the fan was turned off (Fig. 5A). For full state estimation, including wind speed estimation (Fig. 5B), we processed sensor data offline in the Python Control Systems Library (101) using our Kalman filter. We did not have information about the helicopter's throttle or torque commands and so assumed that they are zeromean disturbance noise. Experiments consisted of flying the helicopter 1- to 2-m downwind of a 50-cm-diameter box fan at a specified height $z_d = 1$ m. After the fan was powered on, the robot was

observed moving downwind a short distance (10 to 20 cm) before stabilizing to a new location. We ran the Kalman filter at the maximum data rate that could be achieved over the Bluetooth communication channel (20 Hz). We used the raw optic flow readings from optic flow sensor (PMW3901, Pixart Imaging Inc., Hinschu, Taiwan). The manufacturer does not disclose the optic flow algorithm this sensor uses.

Supplementary Materials

This PDF file includes: Materials and Methods Figs. S1 to S3 Tables S1 to S3 References (106–108)

REFERENCES AND NOTES

- A. M. Flynn, Gnat robots (and how they will change robotics), in *IEEE Micro Robots and Teleoperators Workshop: An Investigation of Micromechanical Structures, Actuators and Sensors*, (IEEE, Institute of Electrical and Electronics Engineers Inc., New York, 1987), vol. 1, p. 158.
- R. A. Brooks, A. M. Flynn, Fast, cheap, and out of control: A robot invasion of the solar system. J. Br. Interplanet. Soc. 42, 478–485 (1989).
- J. M. James, V. Iyer, Y. M. Chukewad, S. Gollakota, S. B. Fuller, Liftoff of a 190 mg laser-powered aerial vehicle: The lightest wireless robot to fly, in *Robotics and Automation (ICRA)*, IEEE Int. Conf., (IEEE, Brisbane, QLD, Australia, 21 to 25 May 2018), pp. 1–8.
- Y. M. Chukewad, J. M. James, A. Singh, S. B. Fuller, Robofly: An insect-sized robot with simplified fabrication that is capable of flight, ground, and water surface locomotion. *IEEE Transact. Robot.* 37, 2025–2040 (2021).
- Y. M. Chukewad, S. B. Fuller, Yaw control of a hovering flapping-wing aerial vehicle with a passive wing hinge. *IEEE Robot. Autom. Lett.* 6, 1864–1871 (2021).
- R. J. Wood, The first takeoff of a biologically inspired at-scale robotic insect. IEEE Trans. Robotics 24, 341–347 (2008).
- K. Y. Ma, P. Chirarattananon, S. B. Fuller, R. J. Wood, Controlled flight of a biologically inspired, insect-scale robot. Science 340, 603–607 (2013).
- X. Yang, Y. Chen, L. Chang, A. A. Calderón, N. O. Pérez-Arancibia, Bee+: A 95-mg fourwinged insect-scale flying robot driven by twinned unimorph actuators. *IEEE Robot. Autom. Lett.* 4, 4270–4277 (2019).
- Y. Chen, S. Xu, Z. Ren, P. Chirarattananon, Collision resilient insect-scale soft-actuated aerial robots with high agility. *IEEE Transact. Robot.* 37, 1752–1764 (2021).
- J. M. Kahn, R. H. Katz, K. S. J. Pister, Next century challenges: Mobile networking for "smart dust", in *Proceedings of the 5th annual ACM/IEEE international conference on Mobile* computing and networking, (1999), pp. 271–278.
- J. Werfel, K. Petersen, R. Nagpal, Designing collective behavior in a termite-inspired robot construction team. Science 343, 754–758 (2014).
- N. Elkunchwar, S. Chandrasekaran, V. Iyer, S. B. Fuller, Toward battery-free free flight: Duty cycled recharging of small drones, in *Int. Conf. Robotics and Intelligent Systems (IROS)* (IEEE, Prague, Czech Republic, 27 September to 1 October 2021).
- W. S. N. Trimmer, Microrobots and micromechanical systems. Sens. Actuators 19, 267–287 (1989).
- G. Caprari, T. Estier, R. Siegwart, Fascination of down scaling-alice the sugar cube robot. J. Micromechatron. 1, 177–189 (2001).
- J. J. Abbott, Z. Nagy, F. Beyeler, B. J. Nelson, Robotics in the small, part i: Microbotics. IEEE Robot. Autom. Mag. 14, 92–103 (2007).
- I. Paprotny, S. Bergbreiter, Small-scale robotics: An introduction, in workshop at the IEEE International Conference on Robotics and Automation, (Springer, 2013), pp. 1–15.
- V. Kumar, N. Michael, Opportunities and challenges with autonomous micro aerial vehicles. Int. J. Rob. Res. 31, 1279–1291 (2012).
- N. O. Pérez-Arancibia, K. Y. Ma, K. C. Galloway, J. D. Greenberg, R. J. Wood, First controlled vertical flight of a biologically inspired microrobot. *Bioinspir. Biomim.* 6, 036009 (2011).
- M. Karásek, F. T. Muijres, C. De Wagter, B. D. W. Remes, G. C. de Croon, A tailless aerial robotic flapper reveals that flies use torque coupling in rapid banked turns. Science 361, 1089–1094 (2018).
- D. S. Drew, K. S. J. Pister, First takeoff of a flying microrobot with no moving parts, in Manipulation, Automation and Robotics at Small Scales (MARSS), 2017 International Conference on (2017), pp. 1–5.

- H. K. H. Prasad, R. S. Vaddi, Y. M. Chukewad, E. Dedic, I. Novosselov, S. B. Fuller, A laser-microfabricated electrohydrodynamic thruster for centimeter-scale aerial robots. *PLOS ONE* 15. e0231362 (2020).
- L. Ristroph, A. J. Bergou, G. Ristroph, K. Coumes, G. J. Berman, J. Guckenheimer, Z. Jane Wang, I. Cohen, Discovering the flight autostabilizer of fruit flies by inducing aerial stumbles. *Proc. Natl. Acad. Sci. U.S.A.* 107, 4820–4824 (2010).
- L. Ristroph, G. Ristroph, S. Morozova, A. J. Bergou, S. Chang, J. Guckenheimer, Z. Jane Wang, I. Cohen, Active and passive stabilization of body pitch in insect flight. J. R. Soc. Interface 10, 20130237 (2013).
- D. Floreano, R. J. Wood, Science, technology and the future of small autonomous drones. *Nature* 521, 460–466 (2015).
- J.-C. Zufferey, D. Floreano, Fly-inspired visual steering of an ultralight indoor aircraft. IEEE Trans. Robot. 22, 137–146 (2006).
- J.-C. Zufferey, A. Klaptocz, A. Beyeler, J.-D. Nicoud, D. Floreano, A 10-gram microflyer for vision-based indoor navigation, in *Intelligent Robots and Systems (IROS)*, 2006 IEEE/RSJ Int. Conf., (IEEE, Beijing, China, 9 to 15 October 2006), pp. 3267–3272.
- J. Serres, D. Dray, F. Ruffier, N. Franceschini, A vision-based autopilot for a miniature air vehicle: Joint speed control and lateral obstacle avoidance. *Auton. Robots* 25, 103–122 (2008).
- J. Conroy, G. Gremillion, B. Ranganathan, J. Humbert, Implementation of wide-field integration of optic flow for autonomous quadrotor navigation. *Auton. Robots* 27, 189–198 (2009).
- A. Beyeler, J.-C. Zufferey, D. Floreano, Vision-based control of near-obstacle flight. Auton. Robots 27, 201–219 (2009).
- C. M Sabo, A. Cope, K. Gurney, E. Vasilaki, J. Marshall, Bio-inspired visual navigation for a quadcopter using optic flow, in *AIAA Infotech@ Aerospace*, (American Institute of Aeronautics and Astronautics, San Diego, CA, 4 to 8 January, 2016), pp. 0404.
- H. D. Escobar-Alvarez, N. Johnson, T. Hebble, K. Klingebiel, S. A. P. Quintero, J. Regenstein, N. A. Browning, R-advance: Rapid adaptive prediction for vision-based autonomous navigation, control, and evasion. *J. Field Robot.* 35, 91–100 (2018).
- P. P. Neumann, V. H. Bennetts, A. J. Lilienthal, M. Bartholmai, J. H. Schiller, Gas source localization with a micro-drone using bio-inspired and particle filter-based algorithms. Adv. Robot. 27, 725–738 (2013).
- J. Burgués, V. Hernández, A. J. Lilienthal, S. Marco, Smelling nano aerial vehicle for gas source localization and mapping. Sensors 19, 478 (2019).
- M. J. Anderson, J. G. Sullivan, T. K. Horiuchi, S. B. Fuller, T. L. Daniel, A bio-hybrid odorguided autonomous palm-sized air vehicle. *Bioinspir. Biomim.* 16, 026002 (2020).
- D. Palossi, A. Loquercio, F. Conti, E. Flamand, D. Scaramuzza, L. Benini, A 64mw dnn-based visual navigation engine for autonomous nano-drones. *IEEE Internet Things J.* 6, 8357–8371 (2019).
- V. Iyer, A. Najafi, J. James, S. Fuller, S. Gollakota, Wireless steerable vision for live insects and insect-scale robots. Sci. Robot. 5, eabb0839 (2020).
- 37. J. J. Koenderink, A. J. van Doorn, Facts on optic flow. *Biol. Cybern.* **56**, 247–254 (1987).
- 38. J. J. Koenderink, Optic flow. Vision Res. 26, 161-179 (1986).
- G. C. de Croon, J. J. G. Dupeyroux, C. De Wagter, A. Chatterjee, D. A. Olejnik, F. Ruffier, Accommodating unobservability to control flight attitude with optic flow. *Nature* 610, 485–490 (2022).
- D. Honegger, L. Meier, P. Tanskanen, M. Pollefeys, An open source and open hardware embedded metric optical flow cmos camera for indoor and outdoor applications, in *Ro-botics and Automation (ICRA)*, 2013 IEEE International Conference on, (IEEE, Oklahoma City, OK, USA, 23 to 26 October 2013), pp. 1736–1741.
- M. W. Mueller, M. Hamer, R. D'Andrea, Fusing ultra-wideband range measurements with accelerometers and rate gyroscopes for quadrocopter state estimation, in 2015 IEEE International Conference on Robotics and Automation (ICRA), (IEEE, Seattle, WA, USA, 26 to 30 May 2015), pp. 1730–1736.
- H. Müller, D. Palossi, S. Mach, F. Conti, L. Benini, Fünfliber-drone: A modular open-platform 18-grams autonomous nano-drone, in *Design, Automation Test in Europe Conference Exhibition (DATE 2021)*, pp. 12–11 (2021).
- B. Friedland, Control system design: An introduction to state-space methods. Courier Corporation (2012).
- Y. Talwekar, V. Iyer, S. B. Fuller, Towards sensor autonomy in sub-gram flying insect-robots:
 A lightweight and power-efficient avionics system, in IEEE Int. Conf. Robotics and Autonomous Systems (ICRA) (2022), pp. 1–7.
- E. F. Helbling, S. B. Fuller, R. J. Wood, Altitude Estimation and Control of an Insect-Scale Robot with an Onboard Proximity Sensor, Springer International Publishing, Cham (2018), pp. 57–69.
- S. Hanson, Z. Foo, D. Blaauw, D. Sylvester, A 0.5 v sub-microwatt cmos image sensor with pulse-width modulation read-out. *IEEE Journal of Solid-State Circuits* 45, 759–767 (2010).

SCIENCE ROBOTICS | RESEARCH ARTICLE

- M.-T. Chung, C.-C. Hsieh, A 0.5 v 4.95 μw 11.8 fps pwm cmos imager with 82db dynamic range and 0.055% fixed-pattern noise, in 2012 IEEE International Solid-State Circuits Conference (IEEE, 2012) pp. 114–116.
- S. Balasubramanian, Y. M. Chukewad, J. M. James, G. L. Barrows, S. B. Fuller, An insect-sized robot that uses a custom-built onboard camera and a neural network to classify and respond to visual input, in *IEEE Int. Conf. Biomedical Rob. and Biomechatronics (BIOROB)*, (IEEE, 2018) pp. 1297–1302.
- P.-E. J. Duhamel, N. O. Pérez-Arancibia, G. L. Barrows, R. J. Wood, Biologically inspired optical-flow sensing for altitude control of flapping-wing microrobots. *Mechatronics, IEEE/ASME Trans. Mechatronics* 18, 556–568 (2013).
- D. Burkhardt, M. Gewecke, Mechanoreception in Arthropoda: The chain from stimulus to behavioral pattern. Cold Spring Harbor. Symposium Quant. Biol. 30, 601–614 (1965).
- P. Argyrakis, A. Hamilton, B. Webb, Y. Zhang, T. Gonos, R. Cheung, Fabrication and characterization of a wind sensor for integration with a neuron circuit. *Microelectron. Eng.* 84, 1749–1753 (2007).
- A. Tagliabue, A. Paris, S. Kim, R. Kubicek, S. Bergbreiter, J. P. How, Touch the wind: Simultaneous airflow, drag and interaction sensing on a multirotor, 2020 (IEEE, Las Vegas, NV, USA, 25 October to 24 January 2020).
- S. B. Fuller, A. Sands, A. Haggerty, M. Karpelson, R. J. Wood, Estimating attitude and wind velocity using biomimetic sensors on a microrobotic bee, in *Robotics and Automation* (ICRA), 2013 IEEE Int. Conf., (IEEE, Karlsruhe, Germany, 6 to 10 May 2013) pp. 1374–1380.
- M. M. Sadeghi, R. L. Peterson, K. Najafi, Hair-based sensors for micro-autonomous systems, in T. George, M. Saif Islam, A. Dutta, eds, Proc. SPIE 8373, Micro- and Nanotechnology Sensors, Systems, and Applications IV, 83731L, (SPIE, 2012), vol. 8373 pp. 83731L.
- K. Rajasekaran, H. Dae Bae, S. Bergbreiter, M. Yu, 3d printed bio-inspired hair sensor for directional airflow sensing, in 2020 IEEE/RSJ International Conference on Intelligent Robots and Systems (IROS), (IEEE, Las Vegas, NV, USA, 24 October 2020 to 24 January 2021) pp. 8945–8950.
- P. Martin, E. Salaün, The true role of accelerometer feedback in quadrotor control, in 2010
 IEEE international conference on robotics and automation, (IEEE, Anchorage Convention
 District, Anchorage, Alaska, USA, 3 to 8 May 2010) pp. 1623–1629.
- R. C. Leishman, J. C. Macdonald, R. W. Beard, T. W. McLain, Quadrotors and accelerometers:
 State estimation with an improved dynamic model. *IEEE Control Syst.* 34, 28–41 (2014).
- Z. E. Teoh, R. J. Wood, A flapping-wing microrobot with a differential angle-of-attack mechanism, in *Robotics and Automation (ICRA)*, 2013 IEEE Int. Conf., (IEEE, Karlsruhe, Germany, 6 to 10 May 2013).
- Z. E. Teoh, S. B. Fuller, P. C. Chirarattananon, N. O. Pérez-Arancibia, J. D. Greenberg, R. J. Wood, A hovering flapping-wing microrobot with altitude control and passive upright stability, in *Intelligent Robots and Systems (IROS)*, 2012 IEEE/RSJ Int. Conf., (IEEE, Vilamoura, Algarve, Portugal, 7 to 12 October 2012) pp. 3209–3216.
- S. B. Fuller, A. D. Straw, M. Y. Peek, R. M. Murray, M. H. Dickinson, Flying *Drosophila* stabilize their vision-based velocity controller by sensing wind with their antennae. *Proc. Natl. Acad. Sci. U.S.A.* 111, E1182–E1191 (2014).
- S. B. Fuller, M. Karpelson, A. Censi, K. Y. Ma, R. J. Wood, Controlling free flight of a robotic fly using an onboard vision sensor inspired by insect ocelli. J. R. Soc. Interface 11, 20140281 (2014).
- S. B. Fuller, Z. E. Teoh, P. Chirarattananon, N. O. Pérez-Arancibia, J. Greenberg, R. J. Wood, Stabilizing air dampers for hovering aerial robotics: Design, insect-scale flight tests, and scaling. *Auton. Robots* 41, 1555–1573 (2017).
- B. Cheng, X. Deng, Translational and rotational damping of flapping flight and its dynamics and stability at hovering. *IEEE Trans. Robot.* 27, 849–864 (2011).
- T. L. Hedrick, B. Cheng, X. Deng, Wingbeat time and the scaling of passive rotational damping in flapping flight. Science 324, 252–255 (2009).
- M. W. Oppenheimer, I. E. Weintraub, D. O. Sigthorsson, D. B. Doman, Control of a minimally actuated biomimetic vehicle using quarter-cycle wingbeat modulation. *J. Guid. Control Dynam.* 38, 1187–1196 (2015).
- J. L. Barron, D. J. Fleet, S. S. Beauchemin, T. A. Burkitt, Performance of optical flow techniques, in *Proceedings 1992 IEEE Computer Society Conference on Computer Vision and Pattern Recognition*, IEEE Computer Society, (1992) pp. 236–237.
- B. D. Lucas, T. Kanade, An iterative image registration technique with an application to stereo vision, in *IJCAI*, (1981), vol. 81, pp. 674–679.
- A. Censi, S. Han, S. B. Fuller, R. M. Murray, A bio-plausible design for visual attitude stabilization. in *Decision and Control (CDC), 2009 IEEE Int. Conf.*, pp. 3513–3520, (IEEE, Shanghai, China, 16 to 19 December 2009).
- B. Hassenstein, W. Reichardt, Systemtheoretische analyse der zeit-, reihenfolgen- und vorzeichenauswertung bei der bewegungsperzeption des Rüsselkäfers chlorophanus. Zeitschrift Fur Naturforsch. 11, 513–524 (1956).
- M. Greiff, Modelling and control of the crazyflie quadrotor for aggressive and autonomous flight by optical flow driven state estimation. Master's thesis (2017).

- J. M. Grasmeyer, M. T. Keennon, Development of the black widow micro air vehicle. Prog. Astronaut. Aeronautic 195, 519–535 (2001).
- J. E. Niven, J. C. Anderson, S. B. Laughlin, Fly photoreceptors demonstrate energy-information trade-offs in neural coding. *PLoS Biol.* 5, e116 (2007).
- A. J. Rutkowski, M. M. Miller, R. D. Quinn, M. A. Willis, Egomotion estimation with optic flow and air velocity sensors. *Biol. Cybern.* 104, 351–367 (2011).
- S. F. Hoerner, Fluid-dynamic drag: Practical information on aerodynamic drag and hydrodynamic resistance, Hoerner Fluid Dynamics, Midland Park, NJ, (1965).
- 75. S. Vogel, Comparative Biomechanics: Life's Physical World. Princeton Univ. Press, (2003).
- J. S. Pulskamp, R. G. Polcawich, R. Q. Rudy, S. S. Bedair, R. M. Proie, T. Ivanov, G. L. Smith, Piezoelectric pzt mems technologies for small-scale robotics and rf applications. MRS Bull. 37, 1062–1070 (2012).
- X. Yan, M. Qi, L. Lin, Self-lifting artificial insect wings via electrostatic flapping actuators, in 2015 28th IEEE International Conference on Micro Electro Mechanical Systems (MEMS), (IEEE, 2015) pp. 22–25.
- P. Bhushan, C. J. Tomlin, Design of the first sub-milligram flapping wing aerial vehicle, in 2019 IEEE 32nd International Conference on Micro Electro Mechanical Systems (MEMS), (IEEE, Seoul, Korea, 27 to 31 January 2019) pp. 2–5.
- 79. J. M. James, S. B. Fuller, A high-voltage power electronics unit for flying insect robots that can modulate wing thrust, in *IEEE Int. Conf. Robotics and Automation (ICRA)*, (2021).
- S. Hollar, A. Flynn, C. Bellew, K. S. J. Pister, Solar powered 10 mg silicon robot, in *The Sixteenth Annual International Conference on Micro Electro Mechanical Systems*, 2003. MEMS-03 Kyoto. IEEE, (IEEE, Kyoto, Japan, 23 January 2003) pp. 706–711.
- K. Sun, T.-S. Wei, B. Y. Ahn, J. Y. Seo, S. J. Dillon, J. A. Lewis, 3d printing of interdigitated liion microbattery architectures. Adv. Mater. 25, 4539–4543 (2013).
- J. B. Bates, N. J. Dudney, B. Neudecker, A. Ueda, C. D. Evans, Thin-film lithium and lithiumion batteries. Solid State Ion. 135, 33–45 (2000).
- M. Duduta, S. de Rivaz, D. R. Clarke, R. J. Wood, Ultra-lightweight, high power density lithium-ion batteries. *Batter. Supercaps* 1, 131–134 (2018).
- G. L. Barrows, C. Neely, Mixed-mode vlsi optic flow sensors for in-flight control of a micro air vehicle, in *Critical Technologies for the future of Computing*, SPIE, (IEEE, the University of Michigan, San Diego, USA, 4 July August, 2000), vol. 4109, pp. 52–63.
- K. Lee, S. Park, S.-Y. Park, J. Cho, E. Yoon, A 272.49 pj/pixel cmos image sensor with embedded object detection and bio-inspired 2d optic flow generation for nano-air-vehicle navigation, in 2017 Symposium on VLSI Circuits, (IEEE, 2017) pp. C294–C295.
- G. Gallego, T. Delbrück, G. Orchard, C. Bartolozzi, B. Taba, A. Censi, S. Leutenegger, A. J. Davison, J. Conradt, K. Daniilidis, D. Scaramuzza, Event-based vision: A survey. *IEEE Trans. Pattern Anal. Mach. Intell.* 44, 154–180 (2022).
- J. R. Serres, F. Ruffier, Optic flow-based collision-free strategies: From insects to robots. Arthropod Struct. Dev. 46, 703–717 (2017).
- N. Franceschini, F. Ruffier, J. Serres, A bio-inspired flying robot sheds light on insect piloting abilities. Curr. Biol. 17, 1–7 (2007).
- G. C. de Croon, Monocular distance estimation with optical flow maneuvers and efference copies: A stability-based strategy. *Bioinspir. Biomim.* 11, 016004 (2016).
- X. Wu, M. W. Mueller, Using multiple short hops for multicopter navigation with only inertial sensors, in 2020 IEEE International Conference on Robotics and Automation (ICRA), (IEEE, Paris, France, 31 May to 31 August 2020) pp. 8559

 –8565.
- F. van Breugel, A nonlinear observability analysis of ambient wind estimation with uncalibrated sensors, inspired by insect neural encoding, in 2021 60th IEEE Conference on Decision and Control (CDC), (IEEE, Austin, TX, USA, 14 to 17 December 2021) pp. 1399–1406.
- S. Han, A. Censi, A. D. Straw, R. M. Murray, A bio-plausible design for visual pose stabilization, in *Intelligent Robots and Systems (IROS), 2010 IEEE/RSJ International Conference on,* (IEEE, San Francisco, CA, 25 to 30 September 2010) pp. 5679–5686.
- G. de Croon, C. De Wagter, T. Seidl, Enhancing optical-flow-based control by learning visual appearance cues for flying robots. *Nat. Mach. Intell.* 3, 33–41 (2021).
- S. B. Fuller, R. M. Murray, A hovercraft robot that uses insect-inspired visual autocorrelation for motion control in a corridor, in *Robotics and Biomimetics (ROBIO)*, 2011 IEEE Int. Conf., (IEEE, Phuket, Thailand, 7 to 11 December 2011) pp. 1474–1481.
- Z. Yu, Y. Talwekar, S. B. Fuller, Visual confined-space navigation using an efficient learned bilinear optic flow approximation for insect-scale robots. in *IEEE Int. Conf. Intelligent Robots and Systems (IROS)*, (IEEE, Kyoto Japan, 23 to 27 October 2022).
- M. H. Dickinson, F.-O. Lehmann, S. P. Sane, Wing rotation and the aerodynamic basis of insect flight. Science 284, 1954–1960 (1999).
- P. Liu, S. P. Sane, J.-M. Mongeau, J. Zhao, B. Cheng, Flies land upside down on a ceiling using rapid visually mediated rotational maneuvers. Sci. Adv. 5, eaax1877 (2019).
- G. Fraenkel, J. W. S. Pringle, Biological sciences: Halteres of flies as gyroscopic organs of equilibrium. *Nature* 141, 919–920 (1938).

SCIENCE ROBOTICS | RESEARCH ARTICLE

- A. L. Eberle, B. H. Dickerson, P. G. Reinhall, T. L. Daniel, A new twist on gyroscopic sensing: Body rotations lead to torsion in flapping, flexing insect wings. J. R. Soc. Interface 12, 20141088 (2015).
- Z. Tu, F. Fei, J. Zhang, X. Deng, An at-scale tailless flapping-wing hummingbird robot. I. design, optimization, and experimental validation. *IEEE Transact. Robot.* 36, 1511–1525 (2020).
- 101. S. B. Fuller, B. Greiner, J. Moore, R. M. Murray, R. van Paasen, R. Yorke, The python control systems library (python-control), in *IEEE Conf. Decision and Control (CDC)*.
- S. B. Fuller, Four wings: An insect-sized aerial robot with steering ability and payload capacity for autonomy. *IEEE Robot. Autom. Lett.* 4, 570–577 (2019).
- J. Förster, System identification of the crazyflie 2.0 nano quadrocopter. B.S. thesis, ETH Zurich, (2015).
- D. Dhingra, Y. M. Chukewad, S. Fuller, A device for rapid, automated trimming of insectsized flying robots. *IEEE Robot. Autom. Lett.* 5, 1373–1380 (2020).
- E. F. Helbling, S. B. Fuller, R. J. Wood, Altitude estimation and control of an insect-scale robot with an onboard proximity sensor, in *Int. Symp. Robotics Res.*, (2015), vol. 2, pp. 57–69.
- 106. W. Reichardt, Movement Perception in Insects, chapter Movement perception in Insects (Academic Press, 1969), pp. 465–493.

- E. Buchner, Photoreception and Vision in Invertebrates, chapter behavioral analysis of spatial vision in insects, Plenum, (1984), pp. 561–621.
- R. O. Dror, D. C. O'Carroll, S. B. Laughlin, Accuracy of velocity estimation by Reichardt Correlators. J. Opt. Soc. Am. A 18, 241–252 (2001).

Acknowledgments: We would like to thank M. Hamer and G. Barrows for insightful discussions and details about the implementations of the Crazyflie's Kalman filter and imaging sensor technology, respectively. Funding: This work was supported by NSF award number FRR-2054850 (S.F.). Author contributions: Conceptualization: S.F. and Z.Y. Methodology: S.F., Z.Y., and Y.P.T. Visualization: S.F. and Z.Y. Funding acquisition: S.F. Project administration: S.F. writing: S.F., Z.Y., and Y.P.T. Software: S.F., Z.Y., and Y.P.T. Investigation: S.F., Z.Y., and Y.P.T. Competing interests: The authors declare that they have no competing interests. Data and materials availability: All data and simulation software are posted to Github using a persistent Digital Object Identifier at https://doi.org/10.5281/zenodo.7324484.

Submitted 6 May 2022 Accepted 1 November 2022 Published 23 November 2022 10.1126/scirobotics.abq8184

Science Robotics

A gyroscope-free visual-inertial flight control and wind sensing system for 10-mg robots

Sawyer FullerZhitao YuYash P. Talwekar

Sci. Robot., 7 (72), eabq8184. • DOI: 10.1126/scirobotics.abq8184

View the article online

https://www.science.org/doi/10.1126/scirobotics.abq8184 Permissions

https://www.science.org/help/reprints-and-permissions

A gyroscope-free visual-inertial flight control and wind sensing system for 10 mg robots Sawyer Fuller,^{1,2*} Zhitao Yu,¹, Yash P. Talwekar¹

¹Department of Mechanical Engineering, University of Washington, Seattle, WA

²Paul G. Allen School of Computer Science, Seattle, WA

* E-mail: minster@uw.edu.

Supplementary materials

Remarks regarding autocorrelation-based optic flow estimation The correlator given in Equation (6) is a slight variation on the Hassenstein-Reichardt (H-R) model for insect optic flow processing (70). The classic H-R model predicts turning response of insects to panoramic visual motion. It uses a first-order low-pass filter instead of a pure delay as part of the derivative computation l_t (above) (106, 107). If the panoramic image is a pure sinusoid of amplitude Aand spatial frequency ω_s moving at speed Ω in rad/s, it can be shown that the output of the correlator in Equation (6) approaches $\Omega_m=A^2\omega_s^2\Omega$ (108) as $\delta\gamma\omega_s$ approaches 0. This shows that the correlator's output increases with increasing optic flow, but also depends on the spatial frequency and amplitude of the image. It was observations of these characteristics in insect behavior that led to introduction of the H-R model (106, 107).

In realistic, broadband images, the correlator responds to the averaged combined effects of the frequency and contrast of the image's constituent Fourier spectra (108). In Lucas-Kanade, the scalar c effectively normalizes out these effects by computing the square of the average spatial gradient of the image pixels. For many conditions of interest, however, c does not change quickly, hence we propose to either compute it only once at the outset, or on an intermittent basis so that it adds negligible additional computation load. Like Lucas-Kanade, a correlator can only

provide a reasonable estimate if the image has contrast, rather than a uniform brightness.

Supplementary methods

Airspeed sensing noise The RMS accelerometer noise at 100 Hz is provided in the datasheet of mCube MC3672 (low-power mode). We calculated the equivalent quantity for the Bosch BMI088 used on the quad-rotor drone by assuming its noise amplitude spectral density (ASD) is flat (white). The root mean squared (RMS) noise σ for a flat bandwidth f is given by $\sigma = ASD\sqrt{f}$.

We observed a factor $\alpha=6.2$ increase in RMS acceleration noise in the helicopter when in flight relative to the datasheet. This is likely the result of rotor and aerodynamics-induced vibration. We assumed that the same amplification factor applies for the NAT robot. To calculate the RMS airspeed noise σ_a [m/s] at the anticipated sampling frequency of f=200 Hz, we used the equation

$$\sigma_a = \alpha g \frac{\sqrt{f}}{\sqrt{100}} \frac{m}{b} \sigma,$$

where g = 9.81 is the gravitational acceleration of the Earth, and m and b are the mass and air drag damping coefficient of the vehicle's dynamics, respectively.

Dynamics model The dynamics given in Equation 19 describe the motion of a hovering aircraft like a robot fly or multi-rotor drone constrained to motion in a 2D plane. They are a subset of the full rigid body dynamics in space, which are given by the Euler-Lagrange equations:

$$\Sigma \mathbf{f} = m\dot{\mathbf{v}}$$

$$\Sigma \mathbf{\tau}' = \mathbf{J}\dot{\omega}' + \omega' \times \mathbf{J}\omega'$$

$$\dot{\mathbf{R}} = \mathbf{R}\omega'^{\times}$$

$$\dot{\mathbf{p}} = \mathbf{v}$$
(21)

where f is any force acting on the vehicle, τ' is any torque acting on the vehicle, v is the velocity and p is the position of the center of mass of the robot in world coordinates, ω' is the angular velocity of the robot, \mathbf{J} is the vehicle's moment of inertia, and \mathbf{R} is the rotation matrix that relates vectors given in body-attached coordinates to world coordinates. For any vector v expressed in world coordinates, v' is the same vector expressed in body-attached coordinates. They are related by $v = \mathbf{R}v'$. Using the special property of rotation matrices that $\mathbf{R}^{-1} = \mathbf{R}^T$, we can also go in the other direction: $v' = \mathbf{R}^T v$. The quantity ω'^{\times} is a 3×3 matrix that performs the cross product operation ω'^{\times} .

Computation and power Table SI gives an estimate of the computation load per pixel of the two optic flow methods. For each method, we tallied the number of clock cycles it takes to perform the primary mathematical operations given by Equations (5) and (6). We neglected edge effects and operations that only needed to be performed once (e.g. multiplication by a constant or division).

This constitutes an approximate measure of the amount of power required. A multiply-accumulate operation typically takes a single cycle for both fixed point and floating point units on common microcontrollers such as the Arm M4 (Arm Technical Reference Manual, available here. Additions also take a single clock cycle, but are much simpler and usually are accompanied by a multiply in a single multiply-accumulate instruction and so have been neglected. Lucas-Kanade requires a single, slower division operation (consuming approximately 10 cycles depending on processor) at the end as part of the 2 × 2 matrix inverse (Equation (5)), but this occurs infrequently and has been neglected.

Table 52 gives an estimate of the number of operations required per step for each of the two LQG controllers. For positive or negative unity entries in the A, B, and C matrices given above, we assume that a multiply operation is not required. The number of entries in the possibly-

	Lucas-Kanade	autocorrelation
multiplies per pixel (1D)	2	1
multiplies per pixel (2D)	6	2
RMS error (1D) (rad/s)	0.044	0.074

Table S1: A comparison of computation requirements and performance in our simulation of the Lucas-Kanade and correlator method

sparse LQG controller gains were estimated by assuming near-zero entries are zero.

Table $\boxed{53}$ gives estimates of the instruction count and power draw of the computations required for the complete control system. In this table, we assumed that two separate copies of the LQG controller are operating simultaneously, one for each of the x-z and y-z planes, respectively. Based on our simulation, we found that it was possible to operate the controller at a 200 Hz update rate; slower update rates led to instability, likely a result of the increasing speed of rotational dynamics at small scale (19), resulting in instability.

We assumed that optic flow computations operated on luminance readings from a camera with a 35×35 square grid of pixels (1225 pixels), the same number used previously in a palm-sized rotorcraft (42). These were used to estimate the optic flow along the body x' and y' directions independently by computing responses along rows and columns of the pixel grid, respectively. We assumed a general-purpose microcontroller such as the 2.6 mg Arm M4-based Max32660 (Maxim Integrated, San Jose, CA USA), which draws approximately 86 μ A per MHz at 1.1 V, or 95 μ W/MHz. We assume it runs at 1 operation per clock cycle and goes into low-power sleep mode in a few microseconds at each time step after computations have completed.

Supplementary figures

component	item	operations
controller	nonzero entries in K (Eq. (17))	6
	integral action computation	1
	total, controller	7
estimator	nonzero, non-unity entries in A	8
	nonzero, non-unity entries in B	0
	nonzero, non-unity entries in C_{AO}	1
	nonzero entries in L (Eq. (12))	9
	total, estimator	18
total (per LQG regulator)		25

Table S2: Estimated number of multiply-accumulate operations needed per update for the LQG regulator.

component	Lucas-Kanade	correlator
x' LQG controller	5000	5000
y' LQG controller	5000	5000
x'- y' optic flow estimation	1,470,000	490,000
total operations/s	1,480,000	500,000
computation power consumed (μ W)	141	48

Table S3: Estimated computation load (in operations/s and power) for combined optic flow and controller computations.

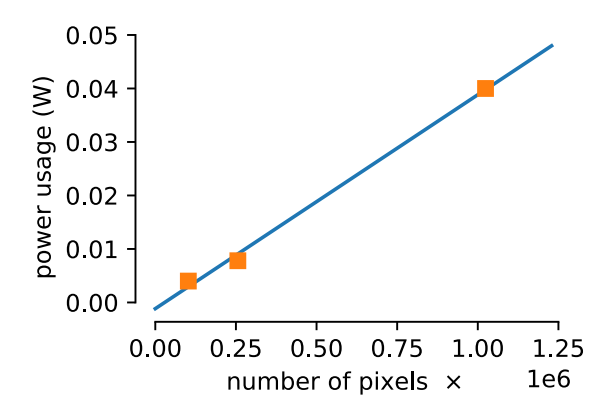


Figure S1: Power scaling per pixel for a commercial imaging sensor family (Himax HM series, Tainan City, Taiwan).

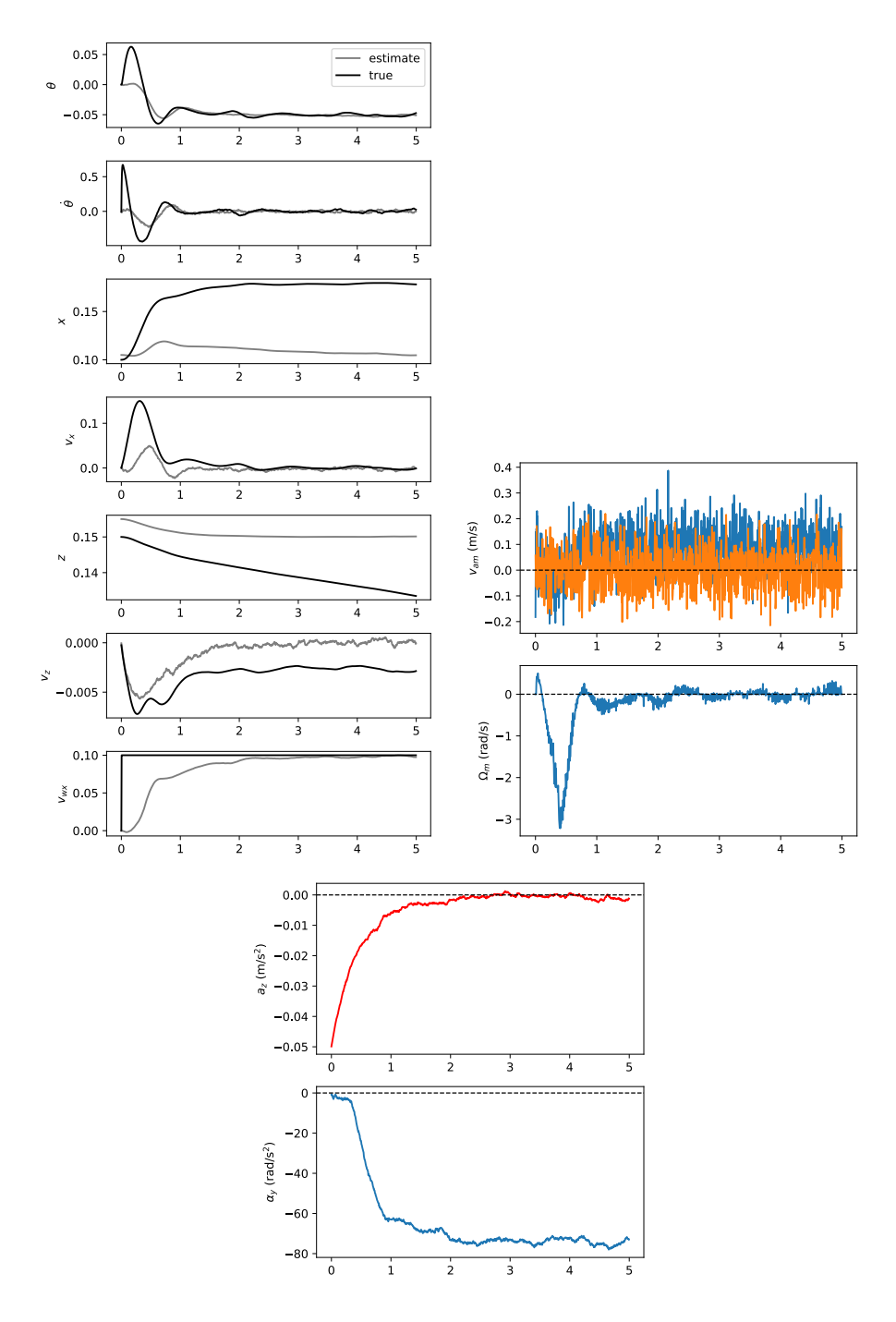


Figure S2: States, measurements, and controller outputs (where a_z is z-axis acceleration \tilde{f}_t and α_y is the y-axis angular acceleration $\tilde{\tau}_y$) during response to step input gust. (Figure 4D) . Units for the state are rad, rad/s, m, m/s, m, m/s, and m/s, respectively.

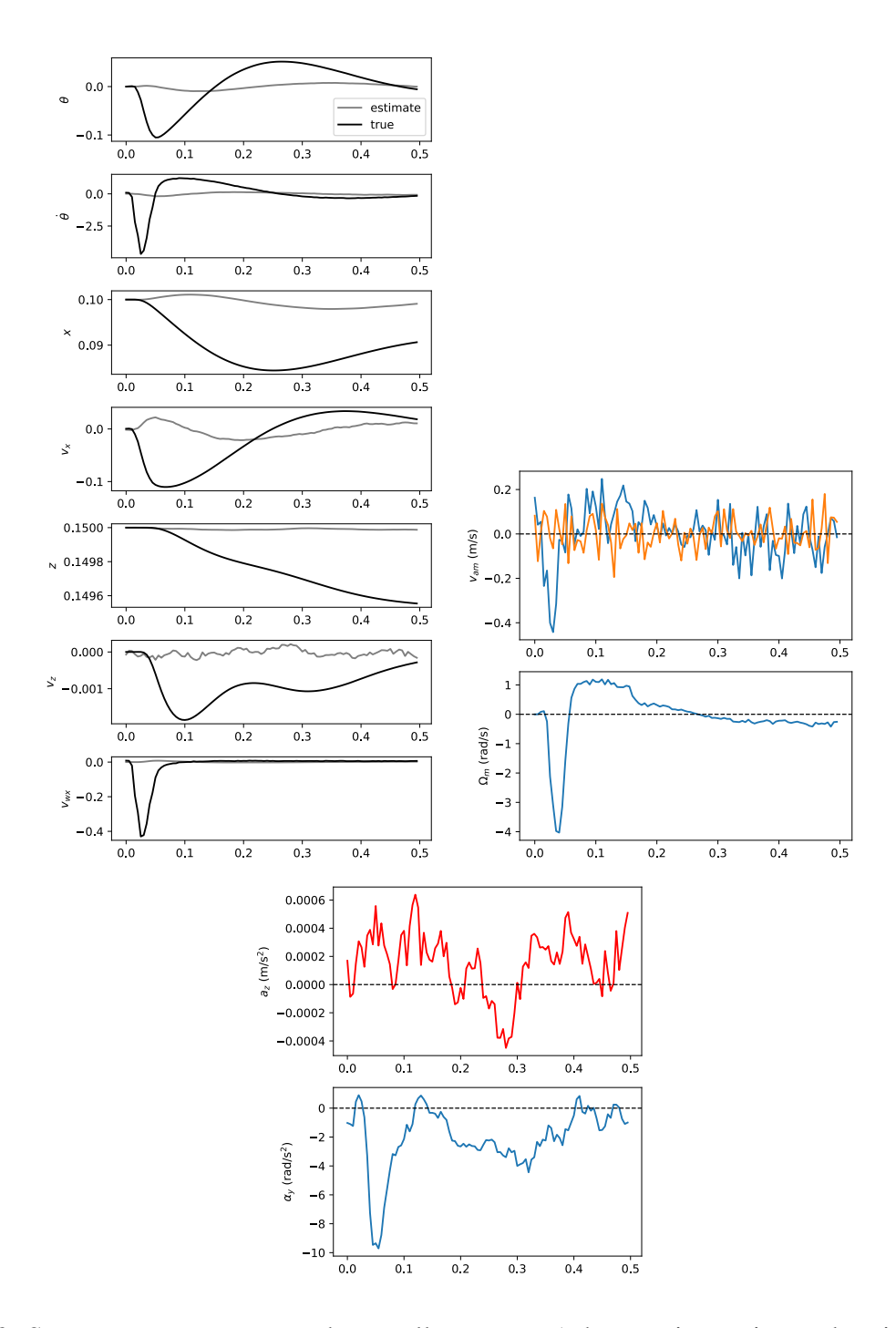


Figure S3: States, measurements, and controller outputs (where a_z is z-axis acceleration \tilde{f}_t and α_y is the y-axis angular acceleration $\tilde{\tau}_y$) during simulated response to impulsive gust (Figure 6). Units for the state are rad, rad/s, m, m/s, m, m/s, and m/s, respectively.